Vortex regeneration mechanism in the self-sustaining process of wall-bounded flows

H. Jane Bae[1]† and Beverley J. McKeon[1]

[1]Graduate Aerospace Laboratories, California Institute of Technology, Pasadena, CA 91125, USA

(Received xx; revised xx; accepted xx)

The streamwise vortex regeneration mechanism in the self-sustaining process (SSP) of wall-bounded turbulence is investigated. Resolvent analysis is used to identify the principal forcing mode which produces the maximum amplification of the velocities in direct numerical simulations (DNS) of the minimal channel for the buffer layer. The identified mode is then projected out from the nonlinear term of the Navier-Stokes equations at each time step from the DNS of the corresponding minimal channel. The results show that the removal of the principal forcing mode is able to inhibit turbulence while removing the subsequent modes instead of the principal one only marginally affects the flow. Analysis of the dyadic interactions in the nonlinear term shows that the contributions toward the principal forcing mode come from a limited number of wavenumber interactions. Using conditional averaging, the flow structures that are responsible for generating the principal forcing mode, and thus the nonlinear interaction to self-sustain turbulence, are identified to be spanwise rolls interacting with oblique streaks. This corroborates previous studies on the vortex regeneration mechanism and characterises the underlying quadratic interactions in the SSP of the minimal channel using resolvent analysis.

1. Introduction

The structure of near-wall turbulence has been extensively investigated over the past half-century. In the vicinity of the wall, the flow is found to be highly organised, consisting of streamwise rolls and low- and high-speed streaks (Kline *et al.* 1967; Smith & Metzler 1983; Blackwelder & Eckelmann 1979) that are involved in a quasi-periodic regeneration cycle (Robinson 1991; Panton 2001; Adrian 2007). However, despite the large effort devoted to the subject, questions still remain in understanding the exact mechanisms by which turbulence self-sustains in wall-bounded turbulent shear flows and the dynamics in which these structures interact is still uncertain.

Important progress was made in the early 1990s using the "minimal flow unit" approach, which revealed that buffer layer streaks can self-sustain even when motions at larger scales are inhibited and that their existence, therefore, relies on an autonomous process (Jiménez & Moin 1991). Hamilton *et al.* (1995) utilised a similar approach for Couette flow, where either certain velocity modes were suppressed to remove streak formation or disturbances were added to allow streak breakdown. Jiménez & Pinelli (1999) further confirmed that this near-wall process is independent of the flow in the logarithmic and outer regions by showing the survival of the near-wall motions in the absence of outer turbulence. The consensus from these studies, along with many others that followed (e.g

† Email address for correspondence: hjbae@caltech.edu

Waleffe 1997), is that the streaks are significantly amplified by the quasi-streamwise vortices via the lift-up effect; the amplified streaks subsequently undergo a rapid streamwise meandering motion, reminiscent of streak instability or transient growth, which eventually results in breakdown of the streaks and regeneration of new quasi-streamwise vortices. Streak formation by streamwise vortices has been extensively documented in the literature (e.g. Bakewell Jr & Lumley 1967; Blackwelder & Eckelmann 1979; Butler & Farrell 1993; Chernyshenko & Baig 2005), and streak breakdown has also received considerable attention (e.g. Kim *et al.* 1971; Hamilton *et al.* 1995; Waleffe 1995; Schoppa & Hussain 2002). Regarding the final component of the SSP, the streamwise vortex regeneration through nonlinear interactions, there is a lack of consensus, and many possible mechanisms have been proposed. Coles (1978) and Sreenivasan (1988) proposed that the streamwise vortices are generated through the Görtler instability mechanism. Vortex–wave interactions between near-planar Tollmien-Schlichting waves and longitudinal vortices have also been considered (Hall & Smith 1990). Jiménez & Moin (1991) proposed the tilting of the vorticity into the streamwise direction as a cause. Nikolaidis *et al.* (2018) cite the parametric interaction between the fluctuating streamwise mean flow and the streamwise varying perturbations as the main mechanism. However, vortex regeneration seems to be a complicated process that arises from nonlinear interactions.

Resolvent analysis (McKeon & Sharma 2010) identifies pairs of response (velocity) and forcing (nonlinear) modes and the corresponding amplification factor from the linearised Navier-Stokes operator and has been successful at identifying the most energetic motions in actual turbulent flows by approximating the nonlinear forcing from the interaction of highly amplified coherent structures. It has been shown that a rank-one approximation captures the characteristics of the most energetic modes of wall-bounded turbulent channels (Moarref *et al.* 2013). We postulate that the principal (most amplified) forcing mode then must have the largest impact on the flow and, in particular, the regeneration cycle, and we show that the turbulence can be suppressed by removing the nonlinear component corresponding to the principal forcing mode.

The paper is organised as follows. We first introduce the method used to identify and remove resolvent forcing modes from the nonlinear term computed from the DNS in §2. We then present the resulting changes in the flow statistics as well as the identification of coherent structures involved in this process in §3. We summarise our findings in §4.

2. Methods

In the following, we consider a channel flow between two parallel walls. The streamwise, wall-normal and spanwise directions are denoted by x, y, and z, respectively. The flow velocities in the corresponding directions are given by u, v, and w. The streamwise and spanwise directions are considered to be periodic. The flow is characterised by the friction Reynolds number $Re_\tau = \delta u_\tau/\nu$, where δ is the half channel height, u_τ is the friction velocity, and ν is the kinematic viscosity.

2.1. *Principal forcing modes*

The incompressible Navier-Stokes equations can be Fourier transformed in homogeneous directions and time and reorganised as

$$-\mathrm{i}\omega\tilde{\boldsymbol{u}} + (\boldsymbol{U}\cdot\hat{\nabla})\tilde{\boldsymbol{u}} + (\tilde{\boldsymbol{u}}\cdot\hat{\nabla})\boldsymbol{U} + \hat{\nabla}\tilde{p} - \frac{1}{Re_\tau}\hat{\Delta}\tilde{\boldsymbol{u}} = \tilde{\boldsymbol{f}}, \quad \hat{\nabla}\cdot\tilde{\boldsymbol{u}} = 0, \tag{2.1}$$

for each (k_x, k_z, ω), where $\tilde{(\cdot)}$ is the Fourier transform in time and space, $\tilde{\boldsymbol{u}}(y; k_x, k_z, \omega) = [\tilde{u}, \tilde{v}, \tilde{w}]^T$ is the velocity fluctuation vector, $\tilde{\boldsymbol{f}}(y; k_x, k_z, \omega) = [\tilde{f}_u, \tilde{f}_v, \tilde{f}_w]^T$ denotes the

nonlinear advection terms, $\boldsymbol{U}(y) = [U, V, W]^T$ is the mean velocity vector averaged over homogeneous directions and time, $\tilde{p}(y; k_x, k_z, \omega)$ is the pressure, $\hat{\nabla} = [\mathrm{i}k_x, \partial_y, \mathrm{i}k_z]^T$, and $\hat{\Delta} = \partial_{yy} - k_x^2 - k_z^2$. Here, the triplet (k_x, k_z, ω) denotes the streamwise and spanwise wavenumbers and the temporal frequency, respectively. Equivalently, we can express this as

$$\begin{bmatrix} \tilde{\boldsymbol{u}}(y; k_x, k_z, \omega) \\ \tilde{p}(y; k_x, k_z, \omega) \end{bmatrix} = \mathcal{H}(k_x, k_z, \omega) \begin{bmatrix} \tilde{\boldsymbol{f}}(y; k_x, k_z, \omega) \\ 0 \end{bmatrix}. \tag{2.2}$$

We refer to the linear operator $\mathcal{H}(k_x, k_z, \omega)$ as the resolvent operator. The singular value decomposition of the resolvent operator returns an ordered basis pair $\{\tilde{\boldsymbol{\psi}}_j, \tilde{\boldsymbol{\phi}}_j\}$ along with the associated singular value σ_j $(\sigma_1 \geqslant \sigma_2 \cdots \geqslant 0)$ which can be used to express the resolvent operator as

$$\begin{bmatrix} \tilde{\boldsymbol{u}}(y; k_x, k_z, \omega) \\ \tilde{p}(y; k_x, k_z, \omega) \end{bmatrix} = \sum_{j=1}^{\infty} \sigma_j(k_x, k_z, \omega) \tilde{\boldsymbol{\psi}}_j(y; k_x, k_z, \omega) \left\langle \tilde{\boldsymbol{\phi}}_j(y; k_x, k_z, \omega), \begin{bmatrix} \tilde{\boldsymbol{f}}(y; k_x, k_z, \omega) \\ 0 \end{bmatrix} \right\rangle, \tag{2.3}$$

where $\langle \cdot, \cdot \rangle$ is the inner product corresponding to the kinetic energy norm, and the basis $\tilde{\boldsymbol{\phi}}_i$ and $\tilde{\boldsymbol{\psi}}_i$ are unitary. We refer to $\tilde{\boldsymbol{\psi}}_j$ as the response modes and $\tilde{\boldsymbol{\phi}}_j$ as the forcing modes. The former identifies the most amplified coherent structures, which are considered to contain most of the energy. The latter are the basis for the nonlinear terms that create the response modes via the linear resolvent operator.

Note that due to the symmetry in the channel flow, the resolvent modes that do not approach the centreline occur in pairs with the same singular value. While any linear combination of two such resolvent modes corresponding to the largest singular value σ_1 can be considered the principal mode, we focus on the principal forcing mode $\tilde{\boldsymbol{\phi}}_1 = [\tilde{\phi}_{1,u}, \tilde{\phi}_{1,v}, \tilde{\phi}_{1,w}, 0]^T$ with the support isolated to one half (bottom) of the channel such that the projection of the resolvent mode will only be directly affected by flow in the bottom half of the channel.

2.2. *Numerical simulation*

The simulations are performed by discretising the incompressible Navier-Stokes equations with a staggered, second-order accurate, central finite-difference method in space (Orlandi 2000), and an explicit third-order accurate Runge-Kutta method for time advancement (Wray 1990). The system of equations is solved via an operator splitting approach (Chorin 1968). Periodic boundary conditions are imposed in the streamwise and spanwise directions, and the no-slip condition is applied at the walls. The resolvent modes were computed using the same staggered, second-order accurate, central finite difference method in the wall-normal direction. The Fourier discretisation in the computation of the resolvent modes in the streamwise and spanwise directions was modified to use the modified wavenumber corresponding to a staggered second-order finite-difference method.

We perform a DNS of the minimal flow unit of an incompressible turbulent channel flow to investigate the SSP in the buffer layer at $Re_\tau \approx 186$. The streamwise, wall-normal, and spanwise domain sizes are $L_x^+ \approx 340$, $L_y^+ \approx 372$ and $L_z^+ \approx 170$, respectively. Jiménez & Moin (1991) showed that simulations in this domain constitute an elemental structural unit containing a single streamwise streak and a pair of staggered quasi-streamwise vortices, which reproduce reasonably well the statistics of the flow in larger domains. The grid spacings in the streamwise and spanwise directions are uniform with $\Delta_x^+ \approx 10.6$ and $\Delta_z^+ \approx 5.3$; non-uniform meshes are used in the wall-normal direction, with the grid stretched toward the wall according to a hyperbolic tangent distribution with $\min(\Delta_y^+) \approx 0.17$ and $\max(\Delta_y^+) \approx 7.6$.

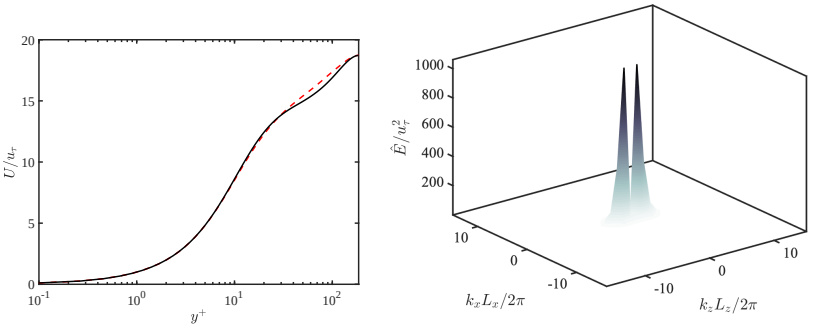

(a) (b)

Figure 1: (a) Mean streamwise velocity profile of the minimal channel (——) compared to the mean velocity profile of the channel flow for the domain size of $12\pi\delta \times 2\delta \times 4\pi$ (- - - -) at $Re_\tau \approx 186$ from Del Alamo & Jiménez (2003). (b) Spectral energy content, $\hat{E}/u_\tau^2$, at $y^+ \approx 15$.

The flow is simulated for more than $50\delta/u_\tau$ after transients for computation of the mean streamwise velocity profile, $U(y)$, shown in Figure 1. Once the mean velocity profile has converged, a separate simulation with the mean $U(y)$ frozen in time by an appropriate forcing at each time step is performed. The mean velocity profile is frozen so that the most amplified resolvent modes remain constant throughout the simulation. It also aligns with the aim of the study, which is to characterise the mechanisms that sustain the turbulent mean state. Once a statistically steady state is reached, the simulation is advanced in time by removing the projection of the Fourier transformed (in homogeneous directions only) nonlinear term, $\hat{\boldsymbol{f}}$, onto $\tilde{\boldsymbol{\phi}}_1$, *i.e.*,

$$\hat{\boldsymbol{g}}_1(y;k_x,k_z) = \left\langle \begin{bmatrix} \hat{\boldsymbol{f}}(y,k_x,k_z) \\ 0 \end{bmatrix}, \tilde{\boldsymbol{\phi}}_1(y;k_x,k_z,\omega) \right\rangle \begin{bmatrix} \tilde{\boldsymbol{\phi}}_{1,u}(y;k_x,k_z,\omega) \\ \tilde{\boldsymbol{\phi}}_{1,v}(y;k_x,k_z,\omega) \\ \tilde{\boldsymbol{\phi}}_{1,w}(y;k_x,k_z,\omega) \end{bmatrix}, \tag{2.4}$$

from $\hat{\boldsymbol{f}}$ for a given (k_x,k_z,ω) at each time step. Projections onto $\tilde{\boldsymbol{\phi}}_i$ are analogously defined as $\hat{\boldsymbol{g}}_i$. Symmetry of the Fourier modes is preserved by also removing $\hat{\boldsymbol{g}}_1^*$, the conjugate of $\hat{\boldsymbol{g}}_1$, from the nonlinear term $\hat{\boldsymbol{f}}(y;-k_x,-k_z)$ at each time step.

For the remainder of the paper, we denote the channel flow simulation with the mean fixed at each time step but no forcing mode removed as the *undamped* case and the simulation with the forcing mode removed as the *damped* case.

2.3. *Choice of target wavenumbers*

As mentioned in the previous section, a choice of the target wavenumbers is required to identify the forcing modes that are removed at each time step. For this, we target the Fourier modes with the most energy content. Figure 1(b) shows the spectral energy content, $\hat{E}(y,k_x,k_z) = 1/2\,(\hat{\boldsymbol{u}}^*\hat{\boldsymbol{u}})$, at $y^+ \approx 15$ as a function of streamwise and spanwise wavenumber. There is a clear peak at $(k_xL_x/2\pi, k_zL_z/2\pi) = (0,\pm1)$. This is consistent with the fact that the domain size of the minimal channel is such that it isolates flow structures to be infinitely long in the streamwise direction and once-periodic in the spanwise direction. Thus, for our analysis, we choose the streamwise and spanwise wavenumbers $(k_xL_x/2\pi, k_zL_z/2\pi) = (0,1)$. The temporal frequency is given as $\omega = 0$, which corresponds to the highest σ_1 for $(k_xL_x/2\pi, k_zL_z/2\pi) = (0,1)$ (Figure 2(a)). Note

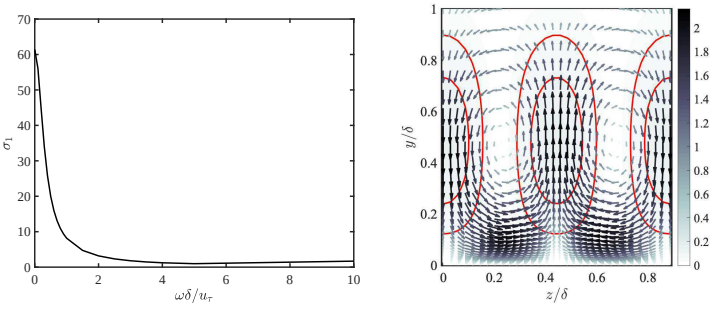

(a) (b)

Figure 2: (a) Principal singular value σ_1 as a function of ω for $(k_xL_x/2\pi, k_zL_z/2\pi) = (0, 1)$. (b) The y-z plane of the principal forcing mode $\tilde{\boldsymbol{\phi}}_1$ for $(k_xL_x/2\pi, k_zL_z/2\pi, \omega\delta/u_\tau) = (0, 1, 0)$. The streamwise component (colour) and the cross-flow component (quiver) are given, with the colour bar indicating magnitude for both components. The contour lines (——) indicate streamwise magnitudes that are 3% and 5% of the maximum cross-flow magnitudes.

that the projection (2.4) includes the contributions from various temporal frequencies apart from $\omega = 0$. However, it ascertains the removal of this particular forcing mode. Also, the singular value associated with $\omega = 0$ is much larger than other temporal frequencies, making the removal of other frequency contents relatively less significant.

The principal forcing modes for this particular frequency–wavenumber triplet are given in Figure 2(b). The forcing mode highlights a pair of streamwise rolls spanning the entire channel half-height. A much weaker streamwise streak whose magnitude ($|\tilde{\phi}_{1,u}|$) is approximately 5% of that of the streamwise rolls, $(\tilde{\phi}^2_{1,v}+\tilde{\phi}^2_{1,w})^{1/2}$, is also present. The values above $y/\delta = 1$ are negligible due to our definition of the principal forcing mode. For the given (k_x, k_z, ω), the principal forcing mode contains the largest energetic contribution under unit broadband forcing (approximately 85%), defined as $\sigma_i^2/\sum_{k=1}^{\infty}\sigma_k^2$ for each $\tilde{\boldsymbol{\phi}}_i$. The subsequent modes $\tilde{\boldsymbol{\phi}}_2$ and $\tilde{\boldsymbol{\phi}}_3$ have an energetic contribution of approximately 12% and 2%, respectively. The large separation in the singular values indicates that the principal forcing mode will be amplified by almost an order of magnitude more than the other forcing modes and thus will be integral in the SSP.

3. Results

3.1. *Time evolution of turbulence kinetic energy and turbulence intensities*

The effect of removing $\hat{\boldsymbol{g}}_1$ can be seen in Figure 3(a) in the form of the turbulence kinetic energy (TKE) evolution in time. It shows that removing $\hat{\boldsymbol{g}}_1$ reduces the TKE significantly. The steady-state root-mean-square (rms) velocity fluctuation profiles for this case are given in Figure 3(b). As expected, the effect of removing the principal forcing term is observed only on the bottom half of the channel where the principal forcing term was isolated, with only minor changes in the statistics in the top half of the channel. At any instance in time of the undamped case, the contribution of $\hat{\boldsymbol{g}}_1$ to the nonlinear advection term, defined as the average ratio of $\int \hat{\boldsymbol{g}}_1^*\hat{\boldsymbol{g}}_1 \mathrm{d}y$ to $\iiint \boldsymbol{f}^2 \mathrm{d}x\mathrm{d}y\mathrm{d}z/2$, is less than 0.9%, and removing the same magnitude randomly from the advection term at each time step had no effect on the first-order statistics, which support the importance of the spatial structure of the mode being projected out to the turbulent flow.

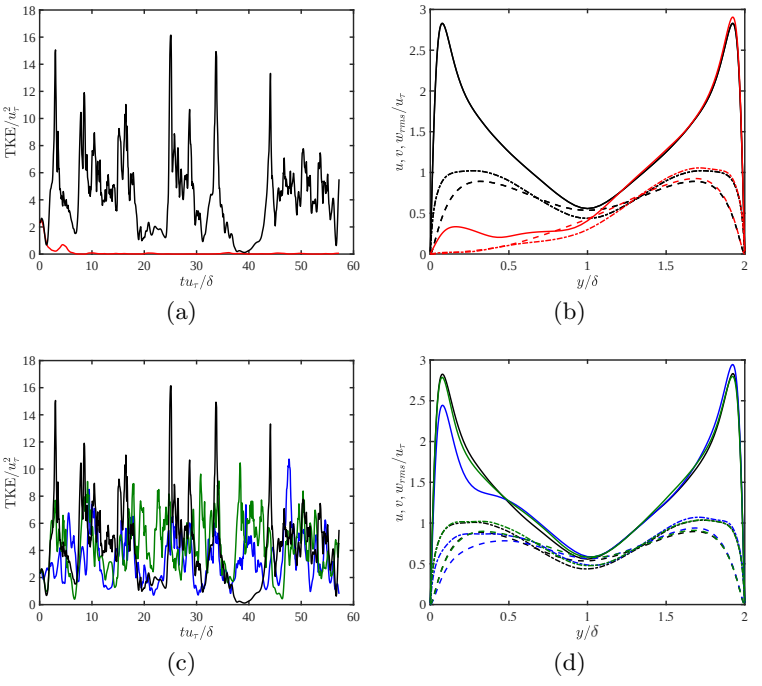

Figure 3: (a) Temporal evolution of TKE at $y^+ \approx 15$ for the damped (——) and the undamped minimal channel (——). (b) Streamwise (——), wall-normal (- - -), and spanwise (-·-·-) rms velocity fluctuations for the damped (red) and the undamped (black) minimal channel. (c,d) Same as (a,b), but removing $\hat{\boldsymbol{g}}_2$ (——) or $\hat{\boldsymbol{g}}_3$ (——) at each time step instead of $\hat{\boldsymbol{g}}_1$.

We also repeat the previous experiment, but removing either $\hat{\boldsymbol{g}}_2$ or $\hat{\boldsymbol{g}}_3$ instead of $\hat{\boldsymbol{g}}_1$. We see that turbulence is sustained in both cases from Figure 3(c), but the extreme peaks in TKE observed in the undamped case are not as prominent. We can also see in Figure 3(d) that while the effect of removing $\hat{\boldsymbol{g}}_2$ still has some impact on the steady-state turbulence intensities, especially around $y^+ \approx 15$, the net change in the statistics is much smaller than that of removing $\hat{\boldsymbol{g}}_1$. Removing $\hat{\boldsymbol{g}}_3$ has no impact on first-order statistics, and similar results are expected of subsequent forcing modes. At any instance of time, the average contribution of $\hat{\boldsymbol{g}}_2$ or $\hat{\boldsymbol{g}}_3$ in the undamped case are statistically similar to the contribution of $\hat{\boldsymbol{g}}_1$ at 0.9% of the total advection term, which supports the impact of the principal forcing mode on the turbulent flow. This demonstrates the capability of resolvent analysis in identifying important fluid structures.

3.2. *Nonlinear interaction*

As demonstrated above, the principal forcing mode $\tilde{\boldsymbol{\phi}}_1$ identifies the most amplified nonlinear interaction and is integral in sustaining turbulence in the near wall cycle. In order to study the nonlinear interactions that produce this term through dyadic interactions, we decompose the nonlinear term as a convolution sum in Fourier space

$$\hat{\boldsymbol{f}}(y;k_x,k_z) = \sum_{k_x',k_z'=-\infty}^{\infty} \left(\hat{\boldsymbol{u}}(y;k_x',k_z')\cdot\hat{\nabla}\right)\hat{\boldsymbol{u}}(y;k_x-k_x',k_z-k_z'), \tag{3.1}$$

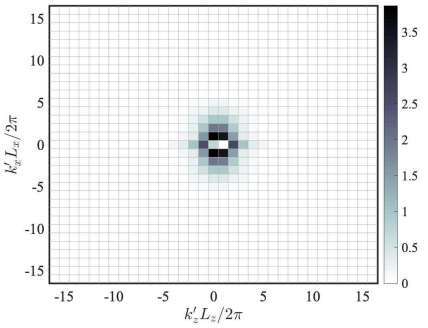

Figure 4: Average contribution of each convolution sum $|\Pi(k_x', k_z')|$ normalised by the total contribution $\left|\sum_{k_x', k_z'} \Pi(k_x', k_z')\right|$ for $k_x L_x/2\pi = 0$ and $k_z L_z/2\pi = 1$.

where $\hat{\nabla} = [\mathrm{i}k_x, \partial_y, \mathrm{i}k_z]^T$. The contribution of each component of the convolution sum toward the projection of the principal forcing term onto $\tilde{\boldsymbol{\phi}}_1$ for any given flow field can be measured as

$$\Pi(k_x', k_z'; k_x, k_z) = \left\langle \begin{bmatrix} \left(\hat{\boldsymbol{u}}(y; k_x', k_z') \cdot \hat{\nabla}\right) \hat{\boldsymbol{u}}(y; k_x - k_x', k_z - k_z') \\ 0 \end{bmatrix}, \tilde{\boldsymbol{\phi}}_1(y; k_x, k_z, \omega) \right\rangle, \tag{3.2}$$

where $(k_x L_x/2\pi, k_z L_z/2\pi) = (0, 1)$ as before. Note that integration over all k_x' and k_z' of $\Pi(k_x', k_z'; k_x, k_z)$ gives the projection coefficient computed in Eq. (2.4). Also, due to incompressibility, Π is symmetric with respect to (k_x, k_z) for each flow field; that is, $\Pi(k_x', k_z'; k_x, k_z) = \Pi(k_x - k_x', k_z - k_z'; k_x, k_z)$. The average spectral map of $|\Pi(k_x', k_z'; k_x, k_z)|$ normalised by the total contribution $|\sum_{k_x', k_z'} \Pi(k_x', k_z'; k_x, k_z)|$ is computed from flow fields of the undamped minimal channel for $k_x L_x/2\pi = 0$ and $k_z L_z/2\pi = 1$ and is depicted in Figure 4. The spectral map identifies two main sources of contribution from the wavenumber pair $(k_x' L_x/2\pi, k_z' L_z/2\pi) = (1, 0)$ and $((k_x - k_x')L_x/2\pi, (k_z - k_z')L_z/2\pi) = (-1, 1)$ and its mirror image in the x-plane, which account for approximately 40% of the total contribution. While the contributions from other wavenumber pairs are not negligible, for the remainder of this paper, we focus on one of the two pairs of wavenumbers to identify the coherent structures responsible for the nonlinear forcing term.

To identify instantaneous flow configurations where the contribution towards $\tilde{\boldsymbol{\phi}}_1$ is strong or weak, we first observe values of $\bar{\Pi}(k_x', k_z') = |\Pi(k_x', k_z')| / \langle \hat{\boldsymbol{f}}(k_x', k_z'), \hat{\boldsymbol{f}}(k_x', k_z') \rangle^{1/2}$, which represents the normalised contribution to the principal forcing term with respect to the total energy of the nonlinear term in the (k_x', k_z') mode, computed from flow fields of the undamped channel. We then determine the mean μ and standard deviation ς of the distribution of $\bar{\Pi}(k_x', k_z')$ over all time instances. The high forcing-intensity events are defined as those with $\bar{\Pi}(k_x', k_z') > \mu + 2\varsigma$ and low forcing-intensity events as those with $\bar{\Pi}(k_x', k_z') < \mu - 2\varsigma$. Both cases consist of approximately 5% of the total events.

The average $\mathcal{F}^{-1}(\hat{\boldsymbol{u}}(k_x', k_z'))$ and $\mathcal{F}^{-1}(\hat{\boldsymbol{u}}(k_x - k_x', k_z - k_z'))$ conditioned to high forcing-intensity events are shown in Figure 5, where $\mathcal{F}^{-1}$ is the inverse Fourier transform. The modes are phase shifted before averaging such that they are phase aligned for the streamwise velocity component at $y^+ \approx 40$. The coherent structures identified by the (k_x', k_z') mode are in the form of a pair of spanwise rolls that is being sheared in the spanwise direction by w. The $(k_x - k_x', k_z - k_z')$ mode show oblique

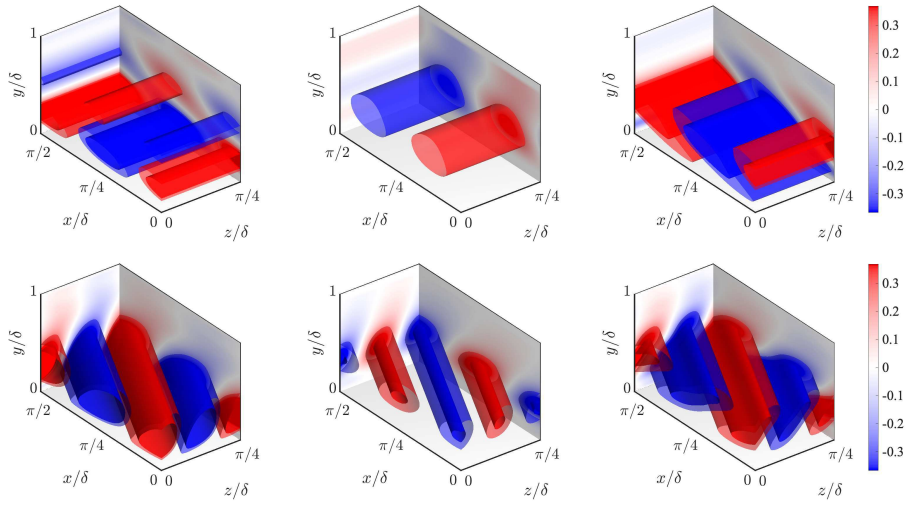

Figure 5: Average $\mathcal{F}^{-1}\left(\hat{u}\right)/u_\tau$ (left), $\mathcal{F}^{-1}\left(\hat{v}\right)/u_\tau$ (centre), $\mathcal{F}^{-1}\left(\hat{w}\right)/u_\tau$ (right) for (k_x', k_z') (top) and $(k_x - k_x', k_z - k_z')$ (bottom) conditioned to high forcing-intensity events. The isosurfaces are 0.41 (solid red), 0.26 (transparent red), −0.26 (transparent blue), and −0.41 (solid blue).

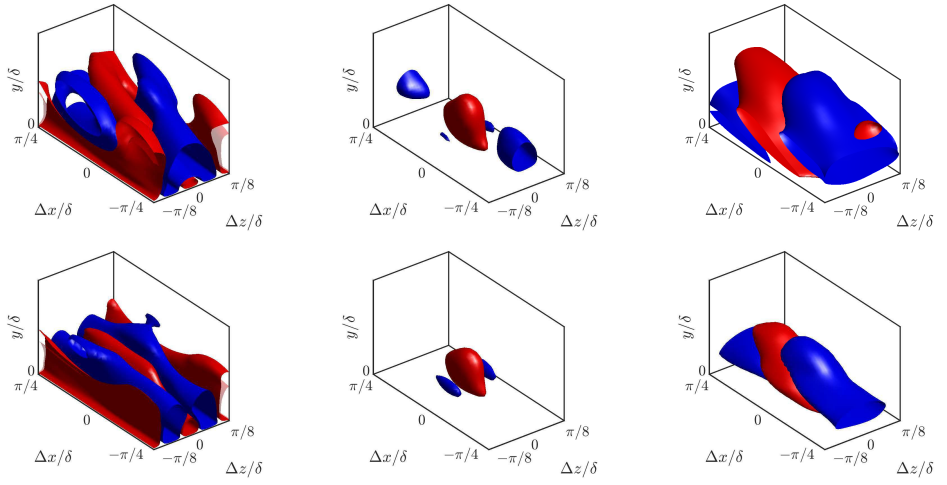

Figure 6: Correlations C_{uu} (left), C_{vv} (center), and C_{ww} (right) conditioned to high forcing-intensity (top) and low forcing-intensity (bottom) events. The isosurfaces are 0.1 (red) and −0.04 (blue).

streaks, which are the components of meandering streaks, with high-speed streaks moving towards the wall and low-speed streaks moving away from the wall, corresponding to sweeps and ejections. Furthermore, the spatial auto-correlation coefficients of the streamwise, wall-normal, and spanwise velocity fluctuations, denoted C_{uu}, C_{vv}, and C_{ww} respectively, are computed, where $C_{uu}(x - x', y, z - z')$ is the correlation between $u(x, y, z)$ and $u(x', y', z')$ conditioned to high forcing-intensity events at $y'^{+} \approx 40$. The correlations shown in the top row of Figure 6 reveal structures very similar to ones

highlighted by the time-averaged $\mathcal{F}^{-1}\left(\hat{\boldsymbol{u}}(k_x', k_z')\right)$ and $\mathcal{F}^{-1}\left(\hat{\boldsymbol{u}}(k_x - k_x', k_z - k_z')\right)$ and resemble spanwise-sheared spanwise rolls (C_{vv} and C_{ww}) with oblique streaks (C_{uu}).

On the contrary, although not shown, $\mathcal{F}^{-1}\left(\hat{\boldsymbol{u}}(k_x', k_z')\right)$ and $\mathcal{F}^{-1}\left(\hat{\boldsymbol{u}}(k_x - k_x', k_z - k_z')\right)$ conditioned to low forcing-intensity events are less coherent for these wave parameters. This can be observed from the conditional correlation in the bottom row of Figure 6, where the streamwise and wall-normal velocities only show structures resembling straight streaks corresponding to wavenumbers $(k_x L_x/2\pi, k_z L_z/2\pi) = (0, 2)$ and no structures resembling oblique streaks or spanwise rolls. Considering the fact that the total kinetic energy distribution for the strong and weak events are similar, these results show that the precursor to the nonlinear interaction that generates the principal forcing mode has more defined coherent structures in the form of spanwise rolls and oblique streaks, which interact to produce the principal forcing mode, which then plays an important role in the SSP of near-wall turbulence. Identifying these precursor events will allow development of new control mechanisms that aim to reduce the production of the resolvent forcing modes essential in sustaining turbulence.

4. Conclusions

We have studied the SSP of wall-bounded turbulence with special emphasis on mechanisms involved in vortex regeneration. For this purpose, we have utilised resolvent analysis to identify the most amplified nonlinear term in the incompressible Navier-Stokes equations and studied the effect of this term on DNS of turbulent channel flow.

Simulations of the minimal channel for the buffer layer with a fixed mean streamwise velocity profile were performed to isolate the structures at a prescribed scale. The most amplified nonlinear term corresponding to the most energetic wavenumber was then computed from the resolvent analysis using the mean velocity profile of the minimal channel simulations. The identified mode was removed from the nonlinear term of a DNS for a minimal channel simulation with a fixed mean velocity profile at each time step. We have shown that the removal of the principal forcing mode leads to suppression of turbulence in the flow. We also applied the removal method for subsequent forcing modes instead, and observed an only marginal decrease in the turbulence intensities, which reinstates the principal forcing mode as the most amplified, and thus the most important, component of the nonlinear term.

In addition, we identified the coherent structures that, through the nonlinear interaction, form the principal forcing mode. The identified structures are in the form of spanwise-sheared spanwise rolls and oblique streaks. The interaction of the two components highlighted here regenerates streamwise vortices, which through the lift-up mechanism amplifies streamwise streaks. These streamwise streaks break down, spawning new generations of meandering streaks and spanwise rolls, completing the SSP. The findings corroborate previous studies on nonlinear interaction of the SSP and allows the characterisation of the the underlying quadratic interactions in the SSP of the minimal channel using resolvent analysis.

This work was funded in part by the Coturb program of the European Research Council. The authors thank Dr. Adrián Lozano-Durán, Dr. Yongseok Kwon, and Dr. Anna Guseva for their insightful comments.

Declaration of Interests. The authors report no conflict of interest.

REFERENCES

Adrian, R. J. 2007. Hairpin vortex organization in wall turbulence. *Phys. Fluids*, **19**(4), 041301.

Bakewell Jr, H. P., & Lumley, J. L. 1967. Viscous sublayer and adjacent wall region in turbulent pipe flow. *Phys. Fluids*, **10**(9), 1880–1889.

Blackwelder, R. F., & Eckelmann, H. 1979. Streamwise vortices associated with the bursting phenomenon. *J. Fluid Mech.*, **94**(3), 577–594.

Butler, K. M., & Farrell, B. F. 1993. Optimal perturbations and streak spacing in wall-bounded turbulent shear flow. *Phys. Fluids A*, **5**(3), 774–777.

Chernyshenko, S. I., & Baig, M. F. 2005. The mechanism of streak formation in near-wall turbulence. *J. Fluid Mech.*, **544**, 99–131.

Chorin, A. J. 1968. Numerical Solution of the Navier-Stokes Equations. *Math. Comput.*, **22**(104), 745–762.

Coles, D. 1978. A model for flow in the viscous sublayer. *Pages 462–475 of: Workshop on coherent structure of turbulent boundary layers.*

Del Alamo, J. C., & Jiménez, J. 2003. Spectra of the very large anisotropic scales in turbulent channels. *Phys. Fluids*, **15**(6), L41–L44.

Hall, P., & Smith, F. T. 1990. Near-planar TS waves and longitudinal vortices in channel flow: nonlinear interaction and focussing. *Pages 5–39 of: Instability and transition.* Springer.

Hamilton, J. M., Kim, J., & Waleffe, F. 1995. Regeneration mechanisms of near-wall turbulence structures. *J. Fluid Mech.*, **287**, 317–348.

Jiménez, J., & Moin, P. 1991. The minimal flow unit in near-wall turbulence. *J. Fluid Mech.*, **225**(4), 213–240.

Jiménez, J., & Pinelli, A. 1999. The autonomous cycle of near-wall turbulence. *J. Fluid Mech.*, **389**, 335–359.

Kim, H. T., Kline, S. J., & Reynolds, W. C. 1971. The production of turbulence near a smooth wall in a turbulent boundary layer. *J. Fluid Mech.*, **50**(1), 133–160.

Kline, S. J., Reynolds, W. C., Schraub, F. A., & Runstadler, P. W. 1967. The structure of turbulent boundary layers. *J. Fluid Mech.*, **30**(4), 741–773.

McKeon, B. J., & Sharma, A. S. 2010. A critical-layer framework for turbulent pipe flow. *J. Fluid Mech.*, **658**, 336–382.

Moarref, R., Sharma, A. S., Tropp, J. A., & McKeon, B. J. 2013. Model-based scaling of the streamwise energy density in high-Reynolds-number turbulent channels. *J. Fluid Mech.*, **734**, 275–316.

Nikolaidis, M.-A., Farrell, B. F., & Ioannou, P. J. 2018. The mechanism by which nonlinearity sustains turbulence in plane Couette flow. *Page 012014 of: J. Phys. Conf. Ser.*, vol. 1001. IOP Publishing.

Orlandi, P. 2000. *Fluid Flow Phenomena: A Numerical Toolkit.* Fluid Flow Phenomena: A Numerical Toolkit. Springer.

Panton, R. L. 2001. Overview of the self-sustaining mechanisms of wall turbulence. *Prog. Aerosp. Sci.*, **37**(4), 341–383.

Robinson, S. K. 1991. Coherent motions in the turbulent boundary layer. *Ann. Rev. Fluid Mech.*, **23**(1), 601–639.

Schoppa, W., & Hussain, F. 2002. Coherent structure generation in near-wall turbulence. *J. Fluid Mech.*, **453**, 57–108.

Smith, C. R., & Metzler, S. P. 1983. The characteristics of low-speed streaks in the near-wall region of a turbulent boundary layer. *J. Fluid Mech.*, **129**, 27–54.

Sreenivasan, K. R. 1988. A unified view of the origin and morphology of the turbulent boundary layer structure. *Pages 37–61 of: Turbulence Management and Relaminarisation.* Springer.

Waleffe, F. 1995. Transition in shear flows. Nonlinear normality versus non-normal linearity. *Phys. Fluids*, **7**(12), 3060–3066.

Waleffe, F. 1997. On a self-sustaining process in shear flows. *Phys. Fluids*, **9**(4), 883–900.

Wray, A. A. 1990. *Minimal-storage time advancement schemes for spectral methods.* Tech. rept. NASA Ames Research Center.